Tensile rotary power transmission model development for airborne wind energy systems

O Tulloch[1], A Kazemi Amiri[1], H Yue[1], J Feuchtwang[1] and R Read[2]

[1]CDT Wind and Marine Energy Systems, Wind Energy and Control Centre, Department of Electronic and Electrical Engineering, Royal College Building, University of Strathclyde, 204 George Street, Glasgow, G1 1XW.
[2]Windswept and Interesting Ltd., 15a Aiginish, Isle of Lewis, Scotland, HS2 0PB.

E-mail: oliver.tulloch@strath.ac.uk, hong.yue@strath.ac.uk

Abstract. Rotary airborne wind energy (AWE) systems are a family of AWE devices that utilise networked kites to form rotors. One such device is the Daisy Kite developed by Windswept and Interesting. The Daisy Kite uses a novel tensile rotary power transmission (TRPT) to transfer power generated at the flying rotor down to the ground. Two dynamic models have been developed and compared; one with simple spring–disc representation, and one with multi–spring representation that can take account of more degrees of freedom. Simulation results show that the angular velocity responses of the two TRPT models are more closely correlated in higher wind speeds when the system shows stiffer torsional behaviour. Another interesting point is the observation of two equilibrium states, when the spring–disc TRPT model is coupled with NREL's AeroDyn. Given the computational efficiency of the simpler model and the high correlation of the results between the two models, the simple model can be used for more demanding simulations.

1. Introduction

Airborne wind energy (AWE) is a novel form of power generation that utilises tethered airborne devices to harness energy from the wind. By using lightweight components and less material AWE systems will be able to access altitudes and locations that are not feasible for current wind turbine technologies. It is also envisaged that AWE will reduce the cost of wind energy [1] and has one of the lowest life time emissions of any power generation technology [2]. The use of tethered wings for power generation was first proposed in the 1970's [3]. The first analytical study was published shortly after [4]. Most AWE studies focus on two generation methods, lift and drag power. Lift power uses a kite, flying in circular or figure of eight flight paths, to reel a tether off a drum on the ground. When the end of the tether is reached, the tether is winched back onto the drum. Devices that use this generation mode are also referred to as pumping cycle systems. Drag power devices use one or more turbines mounted on a kite, as the kite flies through the air, again in circular or figure of eight patterns, power is generated. This power is then transmitted through the tether to a ground station. There are over 60 organisations currently involved in AWE research with these two generation methods dominating the industry [5, 6]. There are multiple prototypes with power ratings in the range of 10–100kW and a handful that are rated at over 100kW. At present there are no commercially available AWE systems and the industry has a technology readiness level of 3–5 [7, 1]. This work focuses on a family of

AWE devices, rotary AWE systems, which are different from lift or drag power generation.

Rotary AWE systems use multiple wings that are networked together to form a rotor, similar to a horizontal axis wind turbine. The rotor is inclined to the incoming wind such that both lift and torque are generated, thus using autorotation which is the self rotation of a rotor without any externally applied torque [8]. The rotor is able to support part of its own weight. There are several rotary systems under development as they have numerous advantages over designs that use lift and drag modes for power generation. The key four advantages are:

(i) Networking wings together constrains an individual wing's flight path. This simplifies the control requirements for each wing and for the system as a whole. There are rotary AWE systems that have reliably generated power with no active control in place [9].

(ii) The networked wings provide the system with a level of redundancy. Therefore rotary systems have fewer single points of failure making them safer and more robust to environmental uncertainties, combined with less requirements for active control, results in rotary systems being more inherently stable compared to lift and drag mode devices.

(iii) Devices that use lift mode generation produce inconsistent power generation during different stages of their operation, and those that use drag mode have heavy electro–mechanical machines on their wing. Rotary systems can be designed to produce continuous power generation while keeping the airborne components as lightweight as possible.

(iv) The networked wings can be configured such that the tether drag is reduced. By reducing the tether drag the overall efficiency of the system is improved [10].

Similar to all AWE systems rotary designs must transmit the energy that is harvested aloft down to the ground station. This can be accomplished either mechanically, as is done by lift mode designs, or electrically, as utilised by drag mode generation. This work has focused on tensile rotary power transmission (TRPT), a unique mechanical transmission, and as a case study has concentrated on the rotary AWE system developed by Windswept & Interesting, the Daisy Kite, shown in Figure 1. Details of the Daisy Kite can be found in [9, 11]. Two other rotary AWE system designs utilise TRPT; Benhaïem and Schmehl use a similar configuration to the Daisy Kite but without intermediate rings between the ground station and flying rotor [12], Beaupoil has developed the open tensegrity shaft that uses straight carbon fibre rods to separate eight tethers [13]. The remainder of this paper deals with modelling and simulation studies of the Daisy Kite system with a focus on TRPT. Section 2 introduces two TRPT representations, the spring–disc and multi–spring models. Section 3 provides a comparison between the two dynamic representations with key features highlighted. Conclusions are given in Section 4.

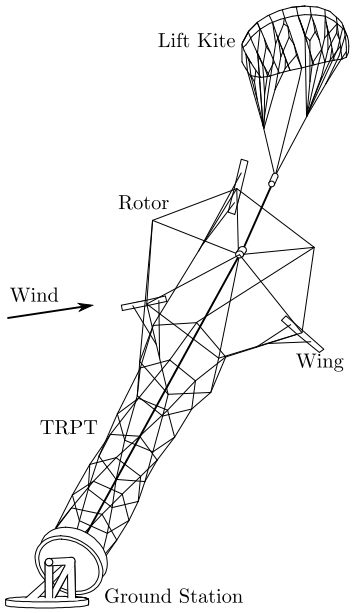

Figure 1: System configuration of the Daisy Kite system

2. Modelling

This section describes two TRPT representations that have been developed based on the Daisy Kite. The Daisy Kite uses a 4.5m diameter 3–wing rotor, each rigid wing has a span of 1m. Its TRPT system has six tethers equally spaced around a series of carbon fibre rings. The 13 rings are positioned along the tube of tethers and increase in radius from 0.3m at the ground

station up to 1.5m at the rotor. This system also uses a lift kite to aid launching, landing and to increase tension within the TRPT when operational. Key components of the Daisy Kite can be seen in Figure 1.

2.1. Spring–disc representation

A spring–disc model is developed for TRPT, assuming each ring within the TRPT is rigid. A single longitudinal section of the TRPT consists of two rings connected by six tethers equally spaced around the circumference of the rings. It is assumed that any force on the TRPT is shared equally among the tethers and that the tethers are straight, do not stretch and are of the same length. The six tethers in a single section can be represented by a single non–linear torsional spring. This model is adapted from analysis by Benhaïem and Schmehl [12].

Figure 2 shows a single TRPT section. Consider points A and B at either end of a tether on adjacent rings with radius R_1 for the lower ring and R_2 for the upper ring. The two rings share the same axis of rotation ($O_1 - O_2$ in Figure 2), which is inclined by elevation angle β to the wind velocity vector V_w, the rings are both orthogonal to the axis of rotation. The three reference frames shown in Figure 2 are as follows:

- In the wind reference frame (x_w, y_w, z_w), x_w is parallel to V_w, y_w is parallel to the ground and z_w perpendicular to the x–y plane, with origin O_1 at the centre of the lower ring.
- In the reference frame for the lower ring (x_a, y_a, z_a) with origin at O_1, x_a lies on the axis of rotation, z_a points towards A and y_a is perpendicular to the x–z plane.
- In the reference frame (x_b, y_b, z_b) with origin at the centre of the upper ring O_2, x_b lies on the axis of rotation, z_b points towards B and y_b is perpendicular to the x–z plane.

Both rings rotate around the axis $O_1 - O_2$ with angular velocity ω and point A lagging behind point B by angle δ. The tether attachment angle γ, the angle between the tether and the tangent to the ring at the attachment point, dictates the amount of torque that is transferred from the tether to the ring or vice versa. Considering the attachment of the tether at points A and B in Figure 2, the tether attachment angles at A (γ_A) and B (γ_B) can be defined by

$$\cos\gamma_A = \frac{R_2}{l_t}\sin\delta \qquad \cos\gamma_B = \frac{R_1}{l_t}\sin\delta \tag{1}$$

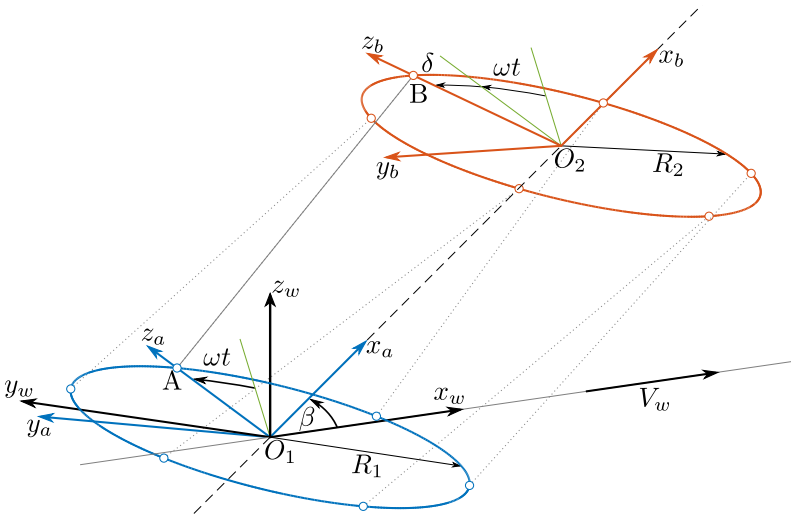

Figure 2: Representation of one section of the TRPT used within the Daisy Kite system.

where l_t is the length of the tethers. As the load is shared equally between all six tethers, (1) represents the tether attachment angles for all six tethers in the TRPT section. The sum of the tangential forces at each tether attachment point gives the overall torque Q that is transferred in this TRPT section.

$$Q = R_1 R_2 F_x \frac{\sin\delta}{\sqrt{l_t^2 - R_1^2 - R_2^2 + 2R_1 R_2 \cos\delta}} \tag{2}$$

where F_x is the overall axial force applied to the section. It can be seen from (2) that the ability of a TRPT section to transfer torque is dependent on its geometry, the axial tension on the section and the torsional deformation δ. The axial tension on the TRPT is a combination of the rotors thrust and the aerodynamic force on the lift kite. The larger this axial tension the more torque the TRPT is able to transmit. If the torsional deformation becomes too large the tethers within the TRPT will cross, at this point the transmittable torque collapses to zero. By differentiating (2) with respect to the torsional deformation (δ) the stiffness of a TRPT section is described by

$$k = \frac{\partial Q}{\partial \delta} = R_1 R_2 F_x \left(\frac{\cos\delta}{\left(l_t^2 - R_1^2 - R_2^2 + 2R_1 R_2 \cos\delta\right)^{\frac{1}{2}}} + \frac{R_1 R_2 \sin^2\delta}{\left(l_t^2 - R_1^2 - R_2^2 + 2R_1 R_2 \cos\delta\right)^{\frac{3}{2}}} \right) \tag{3}$$

The stiffness given by (3) is used within the spring–disc model to represent the torsional stiffness of each TRPT section, these are used to define the system's stiffness matrix at a given operating point. The tether drag is accounted for using the aerodynamic forces set out by Dunker [14]. In the model, each tether is split in half to form two segments, the tether drag associated with each segment is applied as a torque loss at the closest ring. Therefore the torque loss applied to each ring is the result of the aerodynamic drag on half the tether above and half the tether below that ring.

For a given elevation angle (β) and system geometry, the equation of motion for the spring–disc model is given in (4), where $\boldsymbol{\theta}$ is the vector of the 13 rings rotational angles, in which each entry associates with a supporting ring; $\mathbf{V}_w$ is the wind speed, $\mathbf{J}$ the rings moments of inertia. $\mathbf{T}_D$ gives the torque loss due to tether drag, $\mathbf{T}_S$ denotes the torque applied by the springs and $\mathbf{T}_{ext}$ the torque of the rotor and generator.

$$\mathbf{J}\ddot{\boldsymbol{\theta}} + \mathbf{T}_D(\mathbf{V}_w, \dot{\boldsymbol{\theta}}, \boldsymbol{\theta}) + \mathbf{T}_S(\boldsymbol{\theta}, F_x) = \mathbf{T}_{ext} \tag{4}$$

In (4) all the torque terms are non–linear functions. The central difference integration scheme, a straight forward and efficient method applicable to non–linear problems, is employed to solve (4).

2.2. Multi–spring representation

To consider more degrees of freedom (DOF) in a single TRPT section, a multi–spring model is proposed. Each of the six tethers are now represented by a separate linear spring, removing the assumption that the tethers do not stretch. Considering six tethers, as in the Daisy kite system, each ring is divided into 6 mass sectors by the attachment points of the tethers. A linear spring is assumed for each mass between the two neighbouring attachment points to model the rotational deformation of the ring. For each ring, there are 6 rotational DOFs ($\theta_{i,j}$) plus one axial DOF (X_i), i ($i = 1, ..., 13$) is the index for each ring and j ($j = 1, ..., 6$) is the index for each mass sector. With this model all the masses on the same ring are constrained to have the same axial position but are free to move around the circumference of the ring independently. A schematic, showing this multi–spring representation of a single TRPT section, can be seen in Figure 3. The

tether drag is described in a similar manner as to the spring–disc model with minor alterations. The resulting torque loss due to tether drag is applied to each mass individually, again the tether drag on half the tether above and half the tether below contributes to the force applied to each mass. As the multi–spring representation includes axial DOFs, the axial component from the aerodynamic forces on the tethers is also included. Due to the more complex nature of the problem, Lagrange equations are utilised to derive the equations of motion of the TRPT. For a given elevation angle and system geometry the equations of motion are given in (5), where $\mathbf{M}$ contains the mass and moments of inertia, $\mathbf{u}$ is the position vector that includes the rotational and axial displacements, $\mathbf{F}_D$ the aerodynamic forces on the tether, $\mathbf{F}_S$ the spring forces and $\mathbf{F}_{ext}$ the forces from the rotor, generator and lift kite. The central difference integration scheme is again employed to solve (5).

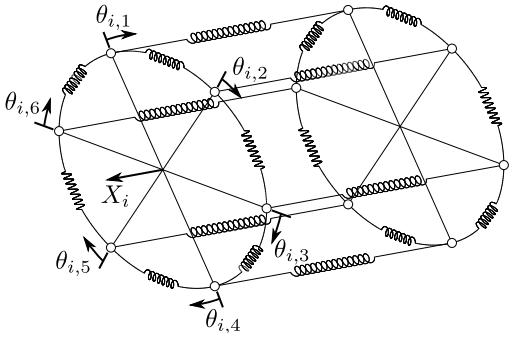

Figure 3: Schematic of a single section of the Daisy Kite's TRPT within the multi–spring representation, the degrees of freedom for one of the rings are shown.

$$\mathbf{M}\ddot{\mathbf{u}} + \mathbf{F}_D(\mathbf{V}_w, \dot{\mathbf{u}}, \mathbf{u}) + \mathbf{F}_S(\mathbf{u}) = \mathbf{F}_{ext} \tag{5}$$

The per unit length stiffness of the springs that represent the tethers and rings are set to 5×10^5 N/m [15] and 4×10^6 N/m [16] respectively. The top ring of the TRPT is also the Daisy Kite's rotor, on which three equally spaced blades are attached at three of the tether attachment points. The aerodynamic torque is applied to only these three masses on the top ring within the multi–spring model.

For both the spring–disc and multi–spring models, the aerodynamics package AeroDyn from NREL's FAST is used to calculate the output from the rotor. AeroDyn uses blade element momentum theory to calculate the aerodynamic forces produced by the rotor. The mass of the rotor is added to the top ring and the mass of the bottom ring is increased by 5kg to account for the rotating components within the ground station. The elevation angle, a parameter that influences the tether drag and rotor performance, is set at 20° for all simulations.

3. Results

A series of simulations are made to compare the rotor responses from the spring–disc and multi–spring models.

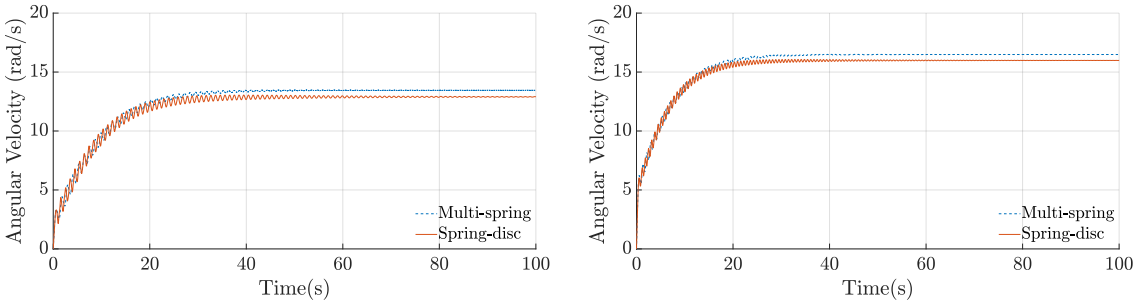

(a) 8m/s (b) 12m/s

Figure 4: Angular velocity of the rotor for the spring–disc and multi–spring representations given constant rotor torque, rotor thrust and generator torque.

3.1. Dynamic Response

For the results given in Figures 4 – 6 the models are not coupled to AeroDyn, however, AeroDyn is used to find values of rotor torque and thrust that correspond to the Daisy Kite's rotor at a steady uniform wind. The generator torque is kept constant such that the system's final state is close to the optimal tip speed ratio of 3.5. Initial simulations using the TRPT representations were run to assess the difference between the two models and to investigate the operation of the Daisy Kite's TRPT. Firstly the steady state angular velocities of both models are compared. Starting from stationary the angular velocity response to a step input wind speed is calculated until the system reaches steady state. Figures 4a and 4b show the angular velocity responses of the top ring under the wind speeds of 8 m/s and 12 m/s respectively, from which it can be seen that the two models produce similar steady angular velocities. At a wind speed of 8 m/s the spring–disc model settles at a velocity of 12.9 rad/s and the multi–spring model at 13.45 rad/s, the difference is 0.55 rad/s. At 12 m/s the spring–disc settles at 16.0 rad/s and the multi–spring at 16.5 rad/s, a difference of 0.5 rad/s is found. This difference could be due to neglecting the axial components of tether drag within the spring–disc representation. It can also be seen from Figure 4 that the transient response of the two models are similar.

To further investigate the dynamic response of both models a variation in generator resisting torque is applied. Figure 5 shows the response of the spring–disc and multi–spring models to a reduction in the torque applied at the generator. Starting from a steady state angular velocity, the generator torque is reduced by 1 Nm for a short period of 0.5 seconds and then returned to its original value. Figures 5a and 5c show the responses at a wind speed of 8 m/s whereas Figures 5b and 5d give the responses at 12 m/s. Only the change in angular velocity from the initial state is shown so that the dynamic response of the two models can be clearly compared. Again the responses of both models are seen to be very similar, the root mean square error (RMSE)

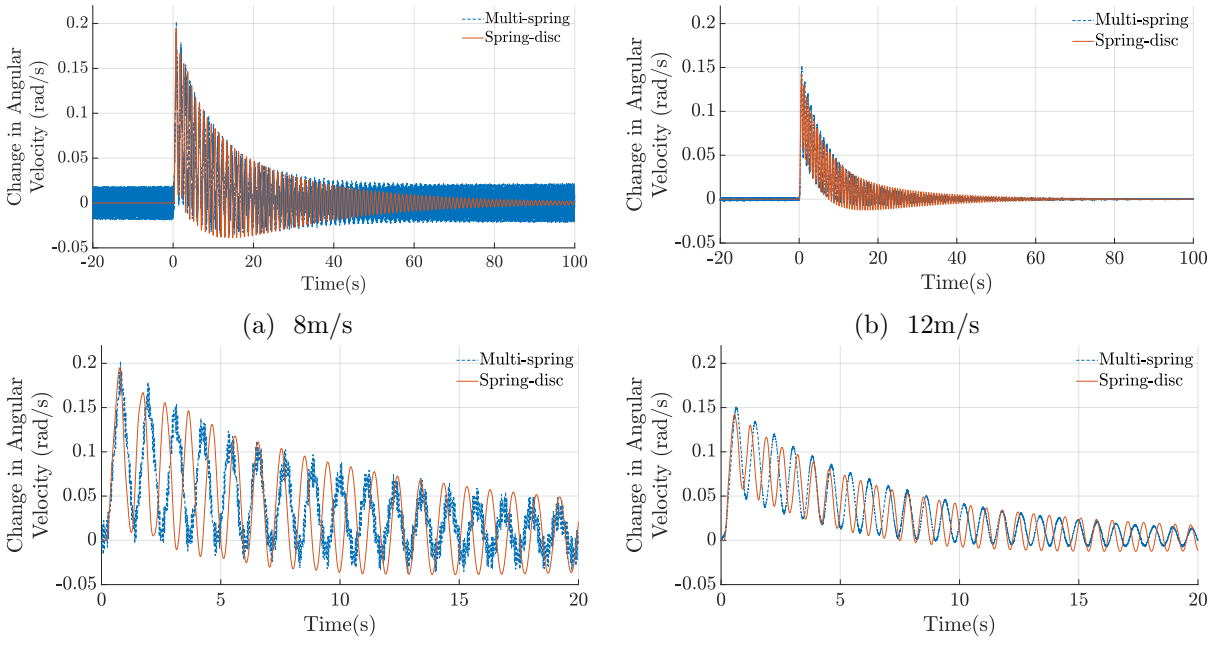

(a) 8m/s (b) 12m/s

(c) magnification of 5a (d) magnification of 5b

Figure 5: Change in angular velocity of the rotor for the spring–disc and multi–spring models with a reduction in generator torque by 1Nm for a period of 0.5 seconds.

Table 1: Selected measures comparing the response of the spring–disc and multi–spring representations for a change in generator torque.

Wind Speed (m/s)	**RMSE**	**Correlation**	**Settling Time** (s)	**Torsional Stiffness** (N/m)
6	0.040	0.36	114	30–40
8	0.031	0.42	81	60–80
10	0.021	0.59	67	90–115
12	0.012	0.79	51	130–170
14	0.007	0.91	32	175–225

and the linear correlation coefficient between the responses of the two models at several wind speeds are shown in Table 1. The settling time, the time taken for the response to remain within 5% of the steady state velocity, and the range of torsional stiffness's, once the steady state is reached, within the spring–disc model are also listed in Table 1.

Observations can be made from Figure 5 and Table 1. It can be seen that the system responds more quickly at higher wind speeds. This is due to the increased torsional stiffness. The equation that determines the stiffness of a single TRPT section given in (3) shows that the stiffness is directly proportional to the axial tension (F_x). At higher wind speeds the thrust from the rotor is larger, increasing the axial tension on the TRPT and therefore the torsional stiffness of each section. This increase in stiffness results in the TRPT responding more quickly to changes in input. It can also be seen that at higher wind speeds the difference between the two TRPT models is smaller and the correlation between them is larger. This is due to the increased aerodynamic damping at higher wind speeds.

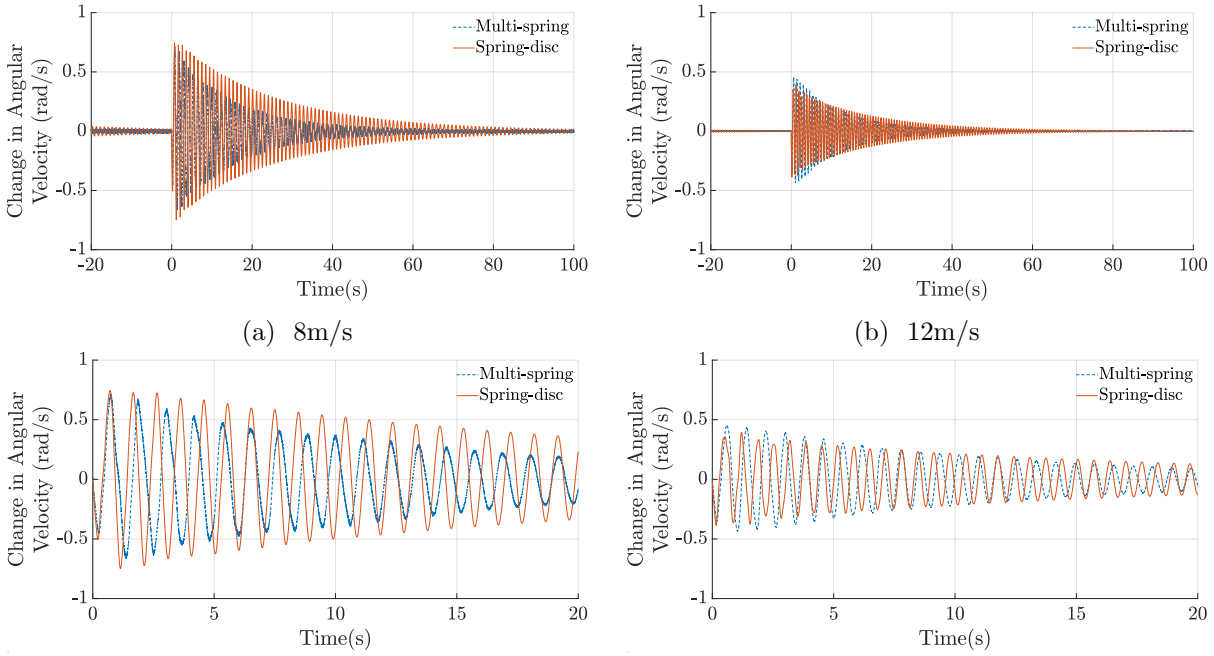

(a) 8m/s

(b) 12m/s

(c) Magnified region of 6a

(d) Magnified region of 6b

Figure 6: Results comparing the change in angular velocity of the rotor for the spring–disc and multi–spring models given an increase in rotor thrust of 100N for a period of 0.5 seconds.

Comparing the multi–spring responses in Figure 5 it can be seen that at a wind speed of 8 m/s there are high frequency fluctuations sitting on the main angular velocity signal whereas at 12 m/s these high frequency fluctuations are reduced. The increased aerodynamic forces experienced by the tethers at larger wind speeds damps out these higher frequency fluctuations. As the spring–disc model has fewer DOFs it does not capture these fluctuations at all. At higher wind speeds there is greater aerodynamic damping therefore the difference between the two models decreases and the correlation between them is greater.

Figure 6 shows the response of the two TRPT models to a variation in axial tension applied at the rotor. The axial tension is increased by 100N for 0.5 seconds before returning to the original value. Figures 6a and 6c show the results for a wind speed of 8 m/s, Figures 6b and 6d for 12 m/s. Again only the difference in angular velocity from the initial state is shown for each models response. The RMSE values for 8m/s and 12 m/s are 0.229 and 0.114, respectively, and the correlation coefficient is 0.003 and 0.019 respectively showing a larger difference between the two models subject to a change in axial tension.

A key difference between the spring–disc and the multi–spring representations is how the axial tension is modelled. In order to determine the torsional stiffness within the spring–disc representation the axial force on each TRPT section must be known, this is assumed to be constant along the length of the TRPT in the spring–disc model. When the rotor thrust or force imposed by the lift kite changes the axial tension along the entire TRPT responds instantly to this change. This results in a swift change in the torsional stiffness of each TRPT section. In contrast the multi–spring representation is able to capture the variation in axial tension along the length of the TRPT, therefore a change in rotor thrust or force driven by the lift kite will propagate along the TRPT. This leads to an increased difference between the responses of the two representations when a change in axial tension is applied in comparison to a change in torque. The ability of the multi–spring model to account for the variation in axial tension suggests that its results are likely to be more accurate. It can however be seen from Figure 5 that for the current Daisy Kite TRPT the two models produce highly similar results. As the length of the TRPT increases and the overall stiffness of the TRPT decreases, the assumption that the axial tension is constant along its length will become less valid. It is expected that the difference between the two TRPT representations will therefore increase for larger scale systems.

3.2. Multiple Steady State Complexity

By coupling the TRPT representations with AeroDyn the interactions between the rotor and TRPT can be analysed. In this simulation the spring–disc model is used for the TRPT. Figure 7 shows the angular velocity of the top ring, the rotor, in the TRPT at a constant uniform wind speed of 8 m/s. A series of simulation results are shown in Figure 7 where the TRPT is given various initial angular velocities, no generator torque is applied. It can be seen that depending on the initial velocity given to the TRPT two different steady angular velocities are possible. This demonstrates there are two equilibrium states for the combined rotor and TRPT system. With a wind speed of 8 m/s the two equilibrium points are

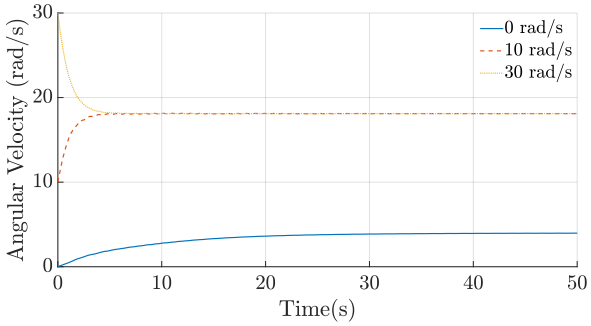

Figure 7: Angular velocity of the TRPT's rotor at a wind speed of 8m/s given different initial angular velocities and no generator torque.

4.5 rad/s and 19 rad/s which correspond to tip speed ratios of 1.2 and 5.3 respectively. The two tip speed ratios identified are consistent for all wind speeds. At a wind speed of 8m/s a threshold of 5 rad/s is identified for the initial value of the angular velocity, below which the lower equilibrium of 4.5 rad/s is reached and above which the higher equilibrium of 19 rad/s reached. Experimental tests on the Daisy Kite have also experienced this phenomenon, whereby power must be applied to the system before higher angular velocities can be achieved.

The multiple equilibrium points observed from this system could be due to the coupling between the rotor and the TRPT system. A steady angular velocity is reached when the rotor torque equals the torque loss due to aerodynamic drag and the generator torque. In the simulations as shown in Figure 7 no generator torque is applied, therefore steady velocities are found when the rotor torque and the torque loss due to tether drag are equivalent. Figure 8 gives the torque coefficient against the tip speed ratio for the rotor alone and the coupled rotor and TRPT system. A torque coefficient of zero occurs when the torque generated by the rotor equals the torque loss within the TRPT. The torque coefficient drops below zero at tip speed ratios of 1.2 and 5.3, matching the equilibrium velocities seen in Figure 7. It can also be seen from Figure 8a that the torque coefficient of the rotor in isolation does not drop below zero until the tip speed ratio is over 6. Given that this phenomenon arises due to the combined rotor and TRPT, it is possible to design the system so that the lower equilibrium velocity does not occur. For example the lower equilibrium velocity would be removed if the same TRPT were used with a rotor that is able to produce more torque, specifically at lower tip speed ratios.

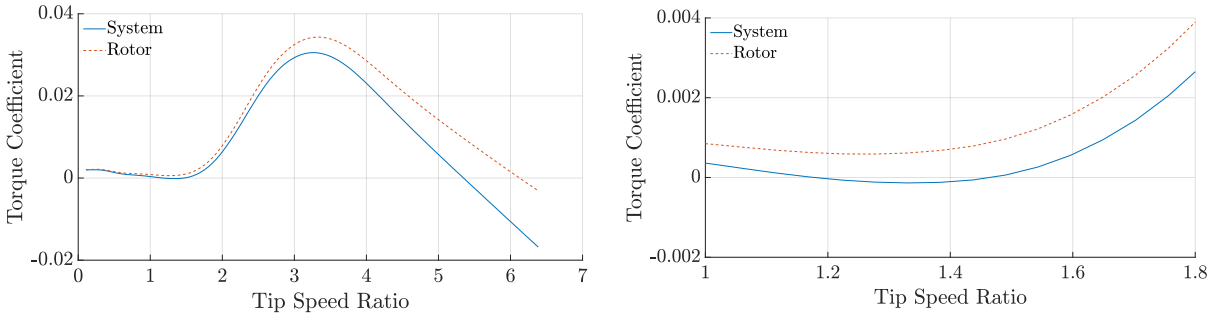

(a) (b) Magnified region of 8a.

Figure 8: Torque coefficient against tip speed ratio for an elevation angle of 20° for the rotor and the full airborne system (rotor and TRPT).

3.3. Computational Performance

Although the multi–spring representation has the advantage of including the varying axial tension, the computational time required is much larger compared to the spring–disc representation. Using MATLAB 2019a and a Intel Core i7–4790 processor a 100 second time horizon takes around 30 seconds to run with the spring–disc model, the multi–spring model requires over two and a half hours. This difference in computational load is mainly due to the time step used within the models. The multi–spring representation requires a time step that is 250 times smaller than the spring–disc representation. This much smaller time step is required due to the stiffness of the multi–spring model. In the spring–disc model the stiffness of the rotational springs are at maximum 225 N/m at a wind speed of 14 m/s whereas in the multi–spring model the per unit length stiffness for the carbon fibre rings is 4×10^6 N/m.

4. Conclusions

Two dynamic representations of the Daisy Kite's TRPT system have been developed. The comparison between the two models has shown that the difference between them is insignificant for the TRPT configuration used by the Daisy Kite. Although the axial tension and the ability of the TRPT to transmit torque are closely related, the response from the two models are better correlated for changes in torque compared to changes in axial tension. This is due to the assumption made within the spring–disc model that the axial tension is constant along the length of the TRPT. It can be generally stated that for an axially stiff TRPT, e.g. systems with a short axial length, the spring–disc model fulfils performance expectations and that for less stiff systems the multi–spring model is more suitable. However, the increased computational time required by the multi–spring model must be considered. At higher wind speeds the torsional stiffness of the TRPT increases which in turn decreases the response time of the TRPT, therefore the system is able to respond more quickly at higher wind speeds. Also at higher wind speeds the difference between the two models is less because of the increased aerodynamic damping which reduces the higher frequency fluctuations within the multi–spring model. When the rotor and spring–disc model are coupled and a constant uniform wind speed applied, the steady state angular velocity has two equilibrium speeds. The initial conditions of the system determines which of the two speeds is reached. The system is in equilibrium when the torque loss within the TRPT and the generator torque are equal to the rotor torque. For the current Daisy Kite design the equilibrium speeds occur at tip speed ratios of 1.2 and 5.3.

Acknowledgments

This research was funded by the EPSRC through the Centre for Doctoral Training in Wind and Marine Energy Systems at the University of Strathclyde, award no. EP/L016680/1. This work is partly supported by the EPSRC through grant EP/R007497/1 and the Natural Environment Research Council UK.

References

[1] Hussen K *et al.* (eds) 2018 *Study on Challenges in the Commercialisation of Airborne Wind Energy Systems* (The European Commission)
[2] Wilhelm S 2018 *Airborne Wind Energy: Advances in Technology Development and Research* ed Schmehl R (Singapore: Springer) chap 30, pp 727–750
[3] Payne P R and McCutchen C 1976 *Self-erecting windmill* US Patent 3987987A
[4] Loyd M L 1980 *Energy* **4**(3) 106–111
[5] Schmehl R (ed) 2018 *Airborne Wind Energy: Advances in Technology Development and Research* (Singapore: Springer)
[6] Schmehl R and Tulloch O (eds) 2019 *The International Airborne Wind Energy Conference 2019: Book of Abstracts* (Delft University of Technology and University of Strathclyde)
[7] Watson S *et al.* 2019 *Renewable and Sustainable Energy Reviews* **113** 109270
[8] Bramwell A R S, Done G and Blamford D 2001 *Bramwell's helicopter dynamics* (Oxford, UK: Butterworth-Heinemann)
[9] Read R 2018 *Airborne Wind Energy: Advances in Technology Development and Research* ed Schmehl R (Singapore: Springer) chap 21, pp 515–537
[10] Schutter J *et al.* 2019 Optimal control of stacked multi-kite systems for utility-scale airborne wind energy *Conf. Decision and Control* (Nice) pp 4865–70
[11] Windswept & interesting ltd URL `https://www.windswept-and-interesting.co.uk/`
[12] Benhaïem P and Schmehl R 2018 *Airborne Wind Energy: Advances in Technology Development and Research* ed Schmehl R (Singapore: Springer) chap 22, pp 539–577
[13] Beaupoil C 2019 *The International Airborne Wind Energy Conference 2019: Book of Abstracts* ed Schmehl R and Tulloch O (University of Strathclyde and Delft University of Technology) pp 146–147
[14] Dunker S 2018 *Airborne Wind Energy: Advances in Technology Development and Research* ed Schmehl R (Singapore: Springer) chap 2, pp 29–56
[15] DSM Dyneema URL `https://www.dsm.com/products/dyneema/en_GB/home.html`
[16] Carbon fibre profiles URL `https://www.carbonfibreprofiles.com/`